

Article

Fe Melting Transition: Electrical Resistivity, Thermal Conductivity, and Heat Flow at the Inner Core Boundaries of Mercury and Ganymede

Innocent C. Ezenwa [†]  and Richard A. Secco ^{*} 

Department of Earth Sciences, University of Western Ontario London, London, ON N6A5B7, Canada

^{*} Correspondence: secco@uwo.ca[†] Now at Institute for Planetary Materials, Okayama University, Misasa, Tottori 682-0193, Japan.

Received: 10 June 2019; Accepted: 12 July 2019; Published: 15 July 2019



Abstract: The electrical resistivity and thermal conductivity behavior of Fe at core conditions are important for understanding planetary interior thermal evolution as well as characterizing the generation and sustainability of planetary dynamos. We discuss the electrical resistivity and thermal conductivity of Fe, Co, and Ni at the solid–liquid melting transition using experimental data from previous studies at 1 atm and at high pressures. With increasing pressure, the increasing difference in the change in resistivity of these metals on melting is interpreted as due to decreasing paramagnon-induced electronic scattering contribution to the total electronic scattering. At the melting transition of Fe, we show that the difference in the value of the thermal conductivity on the solid and liquid sides increases with increasing pressure. At a pure Fe inner core boundary of Mercury and Ganymede at ~5 GPa and ~9 GPa, respectively, our analyses suggest that the thermal conductivity of the solid inner core of small terrestrial planetary bodies should be higher than that of the liquid outer core. We found that the thermal conductivity difference on the solid and liquid sides of Mercury’s inner core boundary is $\sim 2 \text{ W(mK)}^{-1}$. This translates into an excess of total adiabatic heat flow of $\sim 0.01\text{--}0.02 \text{ TW}$ on the inner core side, depending on the relative size of inner and outer core. For a pure Fe Ganymede inner core, the difference in thermal conductivity is $\sim 7 \text{ W(mK)}^{-1}$, corresponding to an excess of total adiabatic heat flow of $\sim 0.02 \text{ TW}$ on the inner core side of the boundary. The mismatch in conducted heat across the solid and liquid sides of the inner core boundary in both planetary bodies appears to be insignificant in terms of generating thermal convection in their outer cores to power an internal dynamo suggesting that chemical composition is important.

Keywords: melting transition; Fe; electrical resistivity; thermal conductivity; high pressure; heat flow; thermal and chemical convection

1. Introduction

The processes of magnetic field generation and sustainability in planetary bodies depend on the composition and thermal state of their cores. Among the rocky planetary bodies with an active dynamo, Mercury has the weakest internally generated magnetic field, with a surface field strength of $\sim 0.3 \mu\text{T}$ or $\sim 1\%$ compared with the Earth’s field. Though a possible remnant crustal magnetization has been suggested [1], a self-sustained dynamo in Mercury’s Fe core is the most plausible source of its global magnetic field [2]. A recent study suggests that a double-diffusive convective regime operates, where both thermal and compositional convection drive the system [3]. Earth-based radar measurements of subtle deviations from the mean resonant spin rate of Mercury demonstrate that Mercury’s mantle is decoupled from its liquid or partially molten core [4–7]. This supports earlier

assertions that Mercury has a molten outer core [8,9]. Recent geodetic constraints on the interior of Mercury from the MESSENGER spacecraft are consistent with a high degree of internal differentiation and a solid inner core with a radius of 0.4–0.7 times the outer core radius [10]. While the role of a solid inner core and its contribution to chemical composition convection in a liquid outer core was recognized long ago for Mercury [9], the possibility of Mercury's weak surface magnetic field resulting from dynamo action in a thin shell geometry has been shown more recently [11]. For the case of Ganymede, although remnant magnetization cannot be completely ruled out as the source of its magnetic field, magneto-convection in its core like that in the Earth has been suggested [12]. However, dynamo action in Ganymede differs from that of the Earth due to the presence of the strong nearby Jovian magnetic field. Thus, the magneto-hydrodynamic equation is variant under the transformation of $\mathbf{B} \rightarrow -\mathbf{B}$ with a directional preference for the self-generated field which could lead to a non-reversing magnetic field unlike the reversing nature of the geomagnetic field [13].

Convection in a terrestrial planetary core can arise from heat transport in excess of the conducted heat (i.e., by thermal convection) or from exsolution and precipitation of core components (i.e., by chemical convection) such as Fe at the inner core boundary, ICB [14], or SiO₂ [15], or MgO [16] at the core-mantle boundary as suggested for Earth. Recent studies have both challenged [17] and supported [18] the MgO precipitation model. There is continuing debate about the relative contributions of thermal vs. chemical convection throughout the thermal and chemical evolution of terrestrial-like planetary cores [19–27]. In a purely thermally driven core, as expected in the early stages of core evolution where a solid inner core and chemical convection are absent, thermal convection is the only source of energy to power the dynamo. Thus, knowing the relative contribution of thermal conduction and thermal convection to thermal transport in the core is essential to understanding the source of energy of a core-generated magnetic field, inner core age, and thermal evolution of the core.

The contribution of conductive heat flow in the core requires the thermal conductivity of core material to be known. Thermal conductivity for metals can be approximated using the Wiedemann-Franz relation if values of electrical resistivity of Fe at high pressure (P) and temperature (T) conditions are known. This approach is often adopted [19–21] over direct measurement of thermal conductivity due to the enormous challenges in maintaining a well-controlled T -gradient in a small sample at very high T and P conditions [22].

Much recent attention in attempts to determine core conductive heat flow is focused on Earth. The electrical resistivity of the Earth's core was estimated to be 350–450 $\mu\Omega\text{cm}$ from analysis of low P static and high P dynamic shock compression data [23,24], leading to calculated values of core thermal conductivity of 30–50 $\text{W}(\text{mK})^{-1}$ that are generally consistent with the only experimental measurements of thermal conductivity made on Fe at core P, T in the diamond anvil cell [25]. However, theoretical [26,27] and experimental investigations [19,20] have suggested a much lower core resistivity (and thermal conductivity values greater than 90 $\text{W}(\text{mK})^{-1}$) for the outer core because of the effect of resistivity saturation at high T .

Theoretical investigation by Wagle and Steinle-Neumann [28] used a thermodynamic model and the Ziman approximation to determine the resistivity of solid and liquid Fe up to core P and T conditions. They found a decreasing resistivity change ($\rho_{\text{liq}} - \rho_{\text{sol}}$) on melting with increasing P . From their experimental resistivity data on *hcp* Fe at high P and room T in the diamond anvil cell (DAC) Gomi et al. [19] asserted that Fe resistivity at core conditions is close to saturation and therefore the resistivity change on melting should be negligible. From their DAC measurements, Ohta et al. [20] reported, ~20% change in Fe resistivity on melting from the *fcc* Fe phase at 51 GPa. However, lower pressure measurements in the multi-anvil press of the T -dependent electrical resistivity of Co up to 5 GPa [29], Ni up to 9 GPa [30], and Fe up to 12 GPa [21] demonstrated an increasing change of resistivity on melting with increasing P . This lower pressure regime is relevant for thermal transport at the ICB in the small planetary bodies Mercury and Ganymede.

From these multi-anvil studies, the resistivity of liquid Co and Ni along their respective P -dependent melting boundaries remained invariant while Fe showed a decreasing trend of resistivity

below the δ - γ -liquid triple point at ~ 5 GPa but then remains constant above the triple point P . Although experimental investigation of electrical resistivity of the α , γ , ϵ phases of Fe at combined static high P and T conditions have been made [20,21,31–33], its behavior through the melting transition is still contentious, hence, a detailed discussion is needed.

Generally, for the $3d$ ferromagnetic metals Fe, Co, and Ni, the weak interaction of d electrons gives rise to an ordered magnetic state characterized by different numbers of electrons with up and down spins. Since the electronic state of a metal can be probed through the investigation of its electrical resistivity, and since electronic state and magnetism in a metal are interwoven [34], electrical resistivity can also provide information about the magnetic state of these metals. We discuss qualitatively our observation of the effect of decreasing magnon-induced electron scattering with increasing P on the T -dependent electrical resistivity of these metals at the solid–liquid transition. In addition, we discuss the possible implications of this behavior on the thermal conductivity and heat flow at the ICB of Mercury and Ganymede.

2. Electronic Scattering in Ferromagnetic Metals

For unfilled d band transition metals, s - d scattering dominates over normal s - s electron scattering as T increases due to the high density of d -band states. This is generally understood in Mott's s - d scattering model [35]. For diamagnetic metals at 1 atm, those with filled d -bands (e.g., Cu, Ag, and Au), the combined results from many studies show that their T -dependent resistivity in the solid state follows a linear dependence on T [36]. Similarly, for some paramagnetic metals at 1 atm (e.g., Pt, Pd, etc), their resistivity follows a near-linear dependence on T [37,38]. However, for the ferromagnetic metals, resistivity follows a T^2 -dependence below the Curie point and T -dependence above the Curie point [39–43]. With increasing T , the increasing phonon and spin-disorder induced scattering (magnon-induced scattering) of the highly mobile s conduction electrons into unfilled d -band states leads to decreased mobility of s electrons and higher resistivity. Below the Curie T , electron scattering is caused by a combination of phonon- and magnon-induced scattering, as well as a contribution from the asymmetry of the Fermi surface (Mott, 1964). Above the Curie T in the paramagnetic state, paramagnon-induced scattering tends toward a constant value while the phonon-induced scattering continues to increase with increasing T and therefore controls the T -dependent resistivity trend. Even if only qualitatively known, the relative contribution of the different scattering mechanisms is important for our study.

Probing band structure effects through resistivity investigation of the ferromagnetic metals under P and T conditions may provide an understanding of the complex electron scattering mechanisms which can occur due to topological features of the Fermi surfaces, Fermi level position, and energy gap between the spin sub-bands (δE_{ex}). Experimental studies mapping the Fermi surfaces of Fe, Co, and Ni have been accomplished primarily through the use of de Hass-van Alphen (dHvA) oscillatory effects [44] along with magnetoresistance investigations that have confirmed the existence of a complicated open orbit topology of the Fermi surfaces of these metals [45–47]. In $3d$ ferromagnetic metals, magnetism is largely caused by electrons in the high density of states $3d$ bands at the Fermi level. Angle-resolved photoemission studies demonstrated that the decrease in δE_{ex} above the Curie T for Fe, Co, and Ni is due to the energy of the spin-down sub-band shifting ~ 2 – 3 times faster than the spin-up sub-band [47–49]. Interestingly, values of δE_{ex} for Fe, Co, and Ni, and the population of the $3d$ -band at ambient conditions correlate with the magnitude of the abrupt change in the electrical resistivity on melting as shown in Figure 1. Ni has the highest number of $3d$ electrons (least number of unoccupied $3d$ states), lowest value of δE_{ex} , and it has the greatest change in resistivity on melting as shown in Figure 1. Fe has the least number of $3d$ electrons (highest number of unoccupied $3d$ states), highest value of δE_{ex} , and it has the smallest change in resistivity [38] on melting. This implies that Fe, having the highest number of unoccupied $3d$ states with the greatest contribution of s - d electron scattering induced by phonons and magnons, should show a smaller change in the resistivity on melting. The small change in the resistivity on melting can thus be explained by the extensive

pre-melting scattering relative to the additional scattering arising from atomic structural change on melting. Conversely, just prior to melting, Ni has the least contribution of scattering from phonon- and magnon-induced s - d electron scattering and therefore shows a larger jump in resistivity arising from the relatively larger scattering contribution on melting due to the effect of atomic structural change.

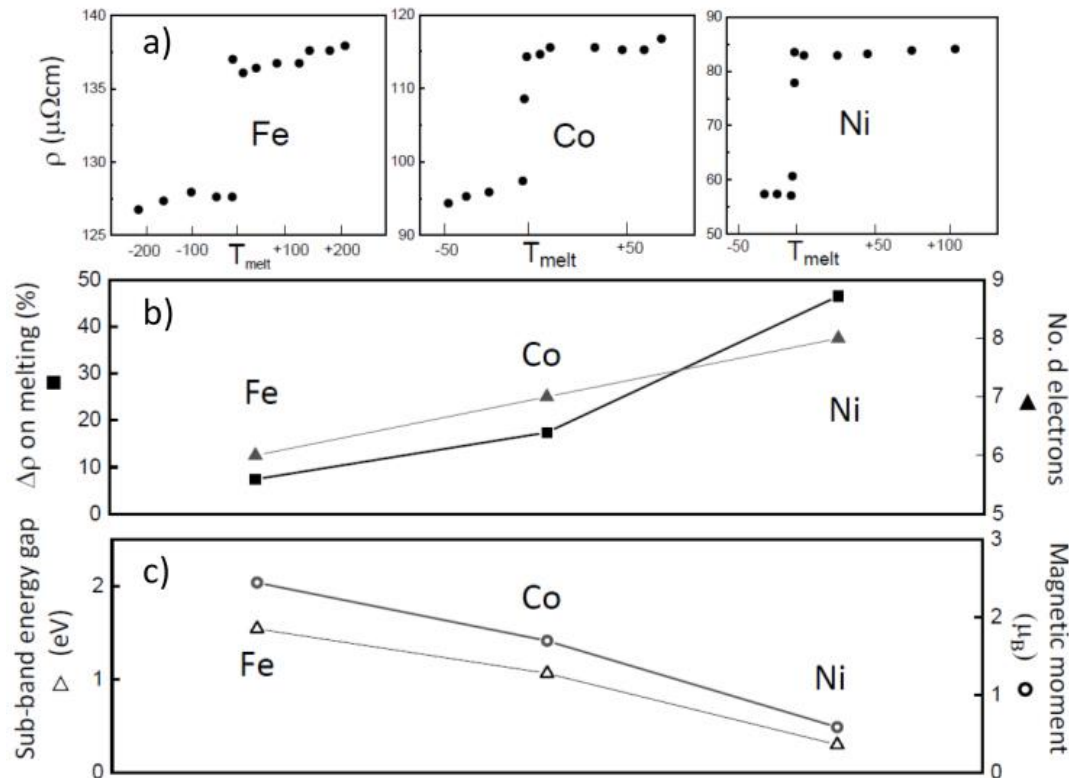


Figure 1. Data of 1 atm of Fe, Co, and Ni. (a) Resistivity discontinuity [38] on melting (note the differences in resistivity scale for Fe, Co, and Ni, whose melting T 's are 1809 K, 1768 K, and 1728 K, respectively); (b) resistivity discontinuity on melting and number of occupied d -electron band, and; (c) sub-band energy gap and magnetic moments [34,50].

Focusing on the magnitude of resistivity of Fe, Co, and Ni in the solid state just prior to melting, the T -dependent resistivity of paramagnetic Fe above the Curie T is similar in trend to the T -dependent resistivity of paramagnetic Pd as phonon-induced scattering dominates in both cases, as shown in Figure 2. On the other hand, an x -ray magnetic circular dichroism study [51] showed that the net magnetic moment of Fe decreases with increasing P and vanishes at ~ 18 GPa at ambient T while both Ni and Co remain ferromagnetic to well over 100 GPa. The increasing population of d -band electrons due to s - d hybridization with increasing P [52–54] will lead to termination of magnetism. It is expected that the relative change in the positions of s and d bands in Fe, Co, and Ni with increasing P control the rate of d -band population and loss/retention of magnetism. Theoretical investigation demonstrated that the non-spin state of Fe is the most energetically favored electronic state at high P [51]. Through P -induced reduction of magnetism and tendency toward spin disorder saturation above the Curie T , these two effects combine to reduce or eliminate the contribution of paramagnon-induced electron scattering in the T -dependent resistivity region of ferromagnetic metals at high P .

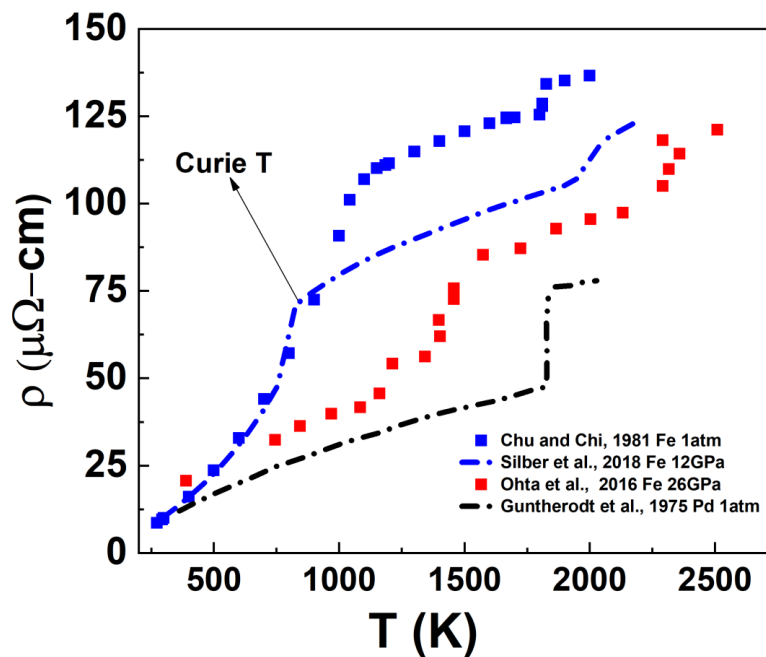


Figure 2. T -dependent electrical resistivity of Fe at different P compared with Pd at 1 atm.

3. Results and Discussion

3.1. Electrical Resistivity and Thermal Conductivity at the Melting Transition

As shown in Figure 3, recent experimental investigations of the T -dependence of resistivity of Co [29], Ni [30], and Fe [21] at high P demonstrate that the effect of P on resistivity is greater in the high T region (T -dependent resistivity) above the Curie T than in the low T region (T^2 -dependent resistivity) below the Curie T . This suggests that magnon-induced scattering is less sensitive to P than is scattering caused by simple phonon scattering or phonon scattering that results in s -electrons being scattered into d -states. This appears intuitively expected as phonon scattering or phonon-induced s - d scattering arise from atomic vibration whereas magnon-induced scattering is operative at the electronic level.

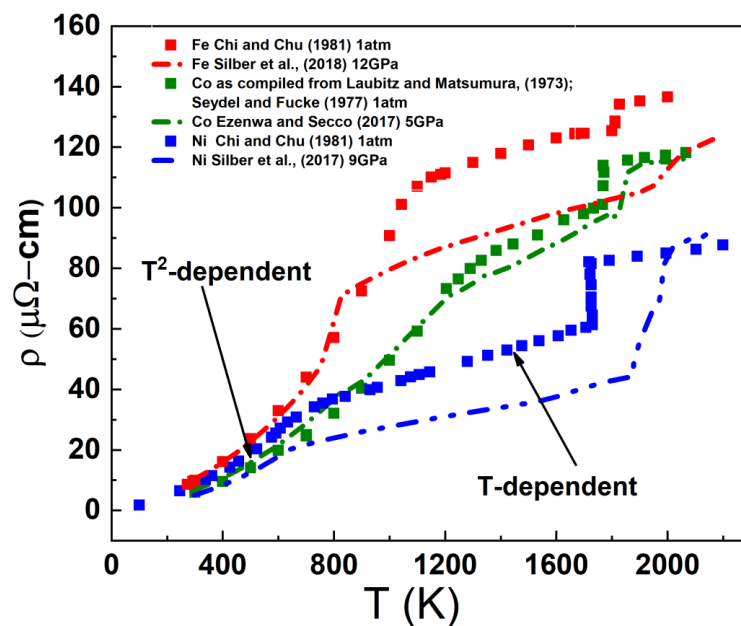


Figure 3. Temperature dependence of resistivity of solid and liquid Fe, Co, and Ni at 1 atm and at various high pressures.

The P -dependence of liquid resistivity of Co and Ni along the melting boundary appears constant up to 5 GPa and 9 GPa, respectively, with values of resistivity on melting (ρ_{liq}) comparable to their corresponding values at 1 atm. The resistivity of Fe on melting decreases up to 5 GPa as it melts from the *bcc* phase but then resistivity on melting remains constant up to 12 GPa as it melts from the *fcc* phase. With a constant value of resistivity on the melting boundary, ρ_{liq} , and a decreasing value of solid resistivity just before melting (ρ_{sol}) with increasing P , $\rho_{liq} - \rho_{sol}$ increases with increasing P up to the maximum pressures investigated in these studies as shown in Figure 4. Although, these data for Fe show an increasing $\rho_{liq} - \rho_{sol}$ with increasing P in this low P range, theoretical calculation [28] up to core P and T show that the $\rho_{liq} - \rho_{sol}$ for Fe melting from the *hcp* phase decreases with increasing P . Further experimental work is needed at higher P to assess the trend of $\rho_{liq} - \rho_{sol}$ for Fe shown here within the context of a larger pressure range.

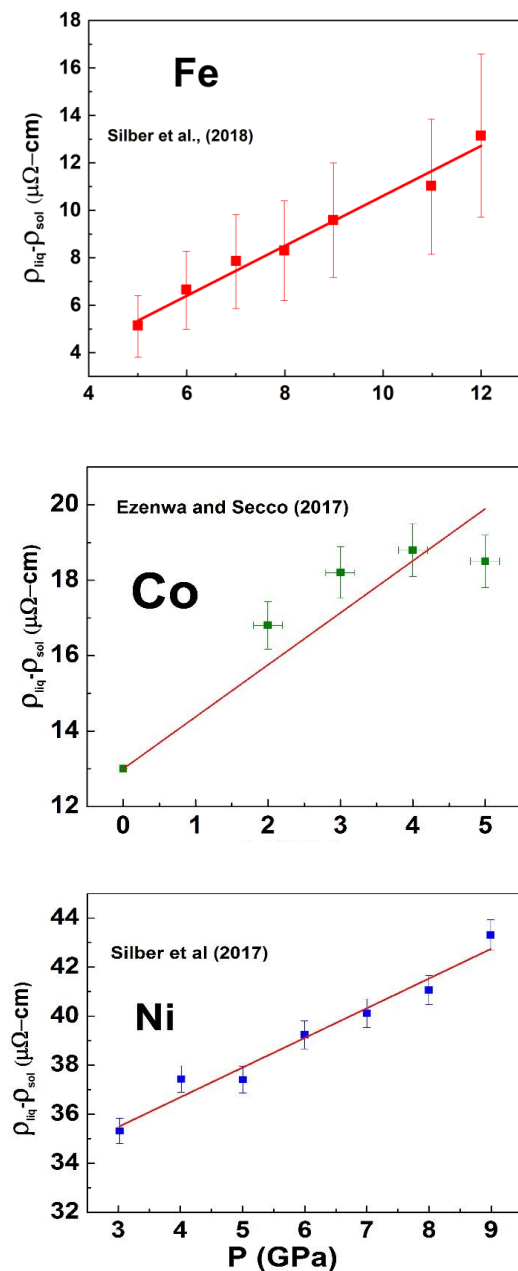


Figure 4. The difference in electrical resistivity value of solid and liquid Fe, Co, and Ni at the melting transition with increasing P . The least squares fits of $\rho_{liq} - \rho_{sol}$ vs. P for Fe, Co, and Ni are, respectively, $(11.33 \pm 3.19) + 0.74 P$, $(12.99 \pm 0.0016) + (1.35 \pm 0.6) P$, and $(31.84 \pm 0.61) + (1.21 \pm 0.1) P$.

Theoretical calculations demonstrate that *d*-resonance scattering dominates the electrical resistivity of unfilled *d*-band liquid metals [55–58]. Experimental study using a flash heating technique in the DAC showed the electrical resistivity of Pt along its high *P* melting boundary is constant [59]. The constancy in the liquid resistivity on the melting boundary may be understood based on the expectation that increasing *P* brings the Fermi level closer to the *d*-resonance site, hence, decreasing conduction electron mobility and increasing resistivity. However, increasing *P* also decreases phonon amplitudes and thus phonon-induced scattering which decreases resistivity. The combined antagonistic effects of *P* on these scattering mechanisms on melting could compensate each other in such a way that resistivity remains constant along the melting boundary, especially in closed packed structures [29,60]. Upon loss of, or reduction in, paramagnon-induced electron scattering at high *P* and *T* conditions, one might infer that the *T*-dependence of resistivity of ferromagnetic metals Fe, Co, and Ni in the solid state could eventually, at high enough *P*, mimic that of paramagnetic metals such as Pt and Pd, at 1 atm [36,37] or perhaps Cu, Ag, Au, and Zn [61–64], where there is a constant paramagnon-induced scattering contribution to its *T*-dependent resistivity.

3.2. Heat Flow at the Inner Core Boundaries of Mercury and Ganymede

The electronic thermal conductivity, k_e , at planetary inner core conditions can be estimated using the Wiedemann-Franz law ($k_e = \frac{LT}{\rho}$) where *L* is the Lorenz number. The total thermal conductivity of metals is dominated by electronic thermal conductivity [65] and one can reasonably assume they are similar in value. Mercury is thought to have a solid inner and liquid outer core with the *P* and *T* conditions at the ICB of ~5 GPa [6] and (1800–2000) K [66], respectively. Parameter values are provided in Table 1. For a pure Fe core in Mercury, using measured resistivity and melting *T* data of Fe at 5 GPa by Silber et al. [21] and the Sommerfeld value ($L_0 = 2.445 \times 10^{-8} \text{ W}\Omega/\text{K}^2$) of the Lorenz number [67], we compute a value of k_e of 39 W(mK)^{-1} for the solid just before melting and 37 W(mK)^{-1} for the liquid side. The errors on these calculated values are mainly due to the errors on the experimentally derived values of ρ_{sol} and ρ_{liq} which are ~5% [21] and the *T* at the ICB; however, we used the same value of 1880 K to calculate both values. The difference in the calculated k_e values suggest ~5% difference in thermal conductivity across the ICB of a pure Fe core in Mercury. While the choice of Lorenz number may also be debated, a single value of *L* is appropriate for calculating k_e on both sides of the ICB which are at a single set of *P,T* conditions. An *L* value different than the one used here will not change the relative values of k_e across the ICB. For Ganymede with P_{ICB} of ~9 GPa [68] and using measured Fe resistivity and melting *T* data by Silber et al. [21], we calculate k_e on the solid side of the ICB in a pure Fe core to be 46 W(mK)^{-1} and on the liquid side to be 39 W(mK)^{-1} , a difference of more than 7%. For Mercury and Ganymede, this analysis suggests that their thermal conductivity on the solid side of their ICB is likely to be higher than on the liquid side of their ICB, but only marginally when errors are considered. This difference is likely to be higher in Ganymede with P_{ICB} of ~9 GPa compared with Mercury with P_{ICB} of ~5 GPa.

The heat flow (*Q*) along the adiabatic *T* gradient in a liquid outer core can be expressed as:

$$Q_{cond} = k \left(\frac{dT}{dz} \right)_{adiabatic} = k \frac{\alpha g T}{C_p} \quad (1)$$

where $\left(\frac{dT}{dz} \right)_{adiabatic}$ is the adiabatic *T* gradient and α , *g*, and C_p are thermal expansion, gravitational acceleration, and heat capacity at constant *P*, respectively. Heat flow transported away from the inner core that exceeds the conducted heat flow in the liquid outer core is transported by thermal convection, which in turn is available for driving a dynamo. Here, we concentrate on the heat transport across the solid and the liquid sides of the ICB of Mercury and Ganymede. At the solid side of Mercury ICB of ~5 GPa, we use a melting *T* for Fe at ~5 GPa of 1880 K [21] and we adopt an average value of $8.9 \times 10^{-5} \text{ K}^{-1}$ for α from the range of values $(6.4\text{--}11.4) \times 10^{-5} \text{ K}^{-1}$ estimated at the top of Mercury's core by Secco [67], a value of 4.0 ms^{-2} for *g* [69], a value of 39 W(mK)^{-1} for k_e , and for C_p a value of

835 J/Kg/K which is assumed independent of P and T [70], we calculate a value of 31 mWm⁻² for the heat flow conducted down the adiabat on the solid side of Mercury ICB. To calculate the total adiabatic heat flow on the solid side of the ICB, we use a total core radius of 2004 km [69] along with the recently obtained estimates of inner core radius of 0.4–0.7 times the outer core radius [10]. These values yield a total adiabatic heat flow of 0.25–0.77 TW. On the liquid side of Mercury ICB, using the calculated k_e of 37 W(mK)⁻¹ and keeping other quantities constant, we calculate a value of 30 mWm⁻² for the conducted heat flow and a range of total adiabatic heat flow of 0.24–0.75 TW. This analysis suggests that for a pure Fe core in Mercury, the difference in the heat conducted along the adiabat across the ICB is small and in the range of 0.01–0.02 TW and likely too small to generate significant thermal convection in the liquid outer core.

Table 1. Parameter values for Mercury and Ganymede used in heat flow calculations *.

Parameter	Mercury	Ref.	Ganymede	Ref.
P_{ICB} —pressure at ICB	5 GPa	[6]	9 GPa	[68]
T_{ICB} —temperature at ICB	1880 K	[66]	2200 K	[71]
L_o —Lorenz number	2.445×10^{-8} W Ω /K ²	[67]	2.445×10^{-8} W Ω /K ²	[67]
k_e solid—electronic thermal conductivity of solid	39 W/m K		46 W/m K	
k_e liquid—electronic thermal conductivity of solid	37 W/m K		39 W/m K	
α —thermal expansion	8.9×10^{-5} K ⁻¹	[67]	4.8×10^{-5} K ⁻¹	[72]
g —gravitational acceleration	4.0 m/s ²	[69]	4.36 m/s ²	
C_p —specific heat	835 J/kg K	[70]	835 J/kg K	[70]
$Q_{\text{cond solid}}$ —conducted heat on solid side of ICB	31 mW/m ²		23 mW/m ²	
$Q_{\text{cond liquid}}$ —conducted heat on liquid side of ICB	30 mW/m ²		19 mW/m ²	
r_{ICB} —radius of ICB	800–1400 km	[10,69]	650 km	[73]
total adiabatic heat flow on solid side of ICB	0.25–0.77 TW		0.12 TW	
total adiabatic heat flow on liquid side of ICB	0.24–0.75 TW		0.10 TW	

* Values in table without references are calculated in this study.

We calculate the heat flow on the solid side of a pure Fe core in Ganymede where P_{ICB} is taken as ~ 9 GPa and $T_{\text{ICB}} \sim 2200$ K [71]. We determine k_e on the solid and liquid side of Ganymede's ICB to be 46 W(mK)⁻¹ and 39 W(mK)⁻¹, respectively. The size of Ganymede inner core, r , is not well determined, however, its core size has been estimated to lie between 650–900 km [73] and we assume an ICB radius of 650 km in our calculations. We estimate gravity $g(r)$ by $4\pi G\rho_c r$ where, G is the gravitational constant, ρ_c is core density ~ 8000 kg/m³ [12] to be 4.36 m/s². From the research of Jeanloz [72], we determine α_{Fe} at 9 GPa to be 4.8×10^{-5} K⁻¹. The melting T of Fe at ~ 9 GPa is ~ 1990 K [21]. Using these parameters in equation 1, we estimate the heat flow on the solid and liquid sides of Ganymede's ICB to be 23 mW/m² and 19 mW/m², respectively. For an inner core radius of ~ 650 km, this yields a total adiabatic heat flow of ~ 0.12 TW and ~ 0.10 TW conducted on the solid and liquid side of Ganymede ICB, respectively. This analysis shows that the larger thermal conductivity difference on the solid and liquid sides of Ganymede's ICB of ~ 7 W(mK)⁻¹ compared to Mercury only causes a difference of ~ 0.02 TW in the heat flow conducted along its adiabat, which is similar to the value for Mercury.

4. Conclusions

The T variation of the electrical resistivity of solid and liquid Fe, Co, and Ni through the melting transition at high P was discussed using experimentally measured data from previous studies. These findings were examined on the basis of reduction of magnon-induced electron scattering (quadratic dependence on T) at high P and T . The scattering of s -electrons to d -states in Fe, Co, and Ni above their Curie T can be related to the increasing phonon-induced scattering to empty d -states (linear dependence on T) and the diminishing relative effect of constant magnon-induced scattering. Relative increases of resistivity on melting in these three metals are self-consistently interpreted within this model. The k_e of solid and liquid at the onset of melting was calculated using the Wiedemann-Franz law with the Sommerfeld value of Lorenz number. These analyses suggest that the thermal conductivity of the solid inner core of small terrestrial planetary bodies could be higher than the liquid outer core. Analysis of the thermal conductivity difference on the solid and liquid side of a pure Fe Mercury and

Ganymede inner core were performed. We found that the thermal conductivity difference on the solid and liquid sides of Mercury's ICB at ~5 GPa is $\sim 2 \text{ W(mK)}^{-1}$, which translates into a difference in total adiabatic heat flow of $\sim 0.01\text{--}0.02 \text{ TW}$, depending on the size of the inner core relative to the outer core. For a pure Fe Ganymede inner core at ~9 GPa, the difference in thermal conductivity is $\sim 7 \text{ W(mK)}^{-1}$, corresponding to difference in total adiabatic heat flow of $\sim 0.02 \text{ TW}$ across its ICB. The cores of both planetary bodies appear to have a difference in conducted heat across their ICB that is insignificant in terms of generating thermal convection to power an internal dynamo suggesting that chemical composition is important.

Author Contributions: I.C.E. conceptualized the work and carried out heat flow analyses; I.C.E. and R.A.S. contributed equally to the interpretations and writing of the manuscript.

Funding: RAS acknowledges the Natural Sciences and Engineering Research Council of Canada (NSERC) (grant number 2018-05021) for research funding.

Acknowledgments: The authors thank Wenjun Yong for comments on the manuscript. ICE thanks Takashi Yoshino for the opportunity to continue research on transport properties applied to planetary bodies at the Institute for Planetary Materials, Okayama University, Misasa, Japan.

Conflicts of Interest: The authors declare no conflict of interest.

References

1. Aharonson, O.; Zuber, M.T.; Solomon, S.C. Crustal remanence in an internally magnetized non-uniform shell: A possible source for Mercury's magnetic field? *Earth Planet. Sci. Lett.* **2004**, *218*, 261–268. [[CrossRef](#)]
2. Christensen, U.R. A deep dynamo generating Mercury's magnetic field. *Nature* **2006**, *444*, 1056–1058. [[CrossRef](#)] [[PubMed](#)]
3. Takahashi, F.; Shimizu, H.; Tsunakawa, H. Mercury's anomalous magnetic field caused by a symmetry-breaking self-regulating dynamo. *Nat. Commun.* **2019**, *10*, 208. [[CrossRef](#)] [[PubMed](#)]
4. Margot, J.L.; Peale, S.J.; Jurgens, R.F.; Slade, M.A.; Holin, I.V. Large longitude libration of Mercury reveals a molten core. *Science* **2007**, *316*, 710–714. [[CrossRef](#)]
5. Margot, J.L.; Peale, S.J.; Solomon, S.C.; Hauck, S.A.; Ghigo, F.D.; Jurgens, R.F.; Yseboodt, M.; Giorgini, J.D.; Padovan, S.; Campbell, D.B. Mercury's moment of inertia from spin and gravity data. *J. Geophys. Res. Planets* **2012**, *117*. [[CrossRef](#)]
6. Hauck, S.A.; Margot, J.L.; Solomon, S.C.; Phillips, R.J.; Johnson, C.L.; Lemoine, F.G.; Perry, M.E. The curious case of Mercury's internal structure. *J. Geophys. Res. Planets* **2013**, *118*, 1204–1220. [[CrossRef](#)]
7. Stark, A.; Oberst, J.; Preusker, F.; Peale, S.J.; Margot, J.L.; Phillips, R.J.; Neumann, G.A.; Smith, D.E.; Zuber, M.T.; Solomon, S.C. First MESSENGER orbital observations of Mercury's librations. *Geophys. Res. Lett.* **2015**, *42*, 7881–7889. [[CrossRef](#)]
8. Ness, N.F.; Behannon, K.W.; Lepping, R.P.; Whang, Y.C.; Schatten, K.H. Magnetic field observations near Mercury: Preliminary results from Mariner 10. *Science* **1974**, *185*, 151–160. [[CrossRef](#)]
9. Stevenson, D.J.; Spohn, T.; Schubert, G. Magnetism and thermal evolution of the terrestrial planets. *Icarus* **1983**, *54*, 466–489. [[CrossRef](#)]
10. Genova, A.; Goossens, S.; Mazarico, E.; Lemoine, F.G.; Neumann, G.A.; Kuang, W.; Sabaka, T.J.; Hauck, I.I.; Smith, D.E.; Solomon, S.C.; et al. Geodetic evidence that Mercury has a solid inner core. *Geophys. Res. Lett.* **2019**, *46*, 3625–3633. [[CrossRef](#)]
11. Stanley, S.; Bloxham, J.; Hutchison, W.E.; Zuber, M.T. Thin shell dynamo models consistent with Mercury's weak observed magnetic field. *Earth Planet. Sci. Lett.* **2005**, *234*, 27–38. [[CrossRef](#)]
12. Kimura, J.; Nakagawa, T.; Kurita, K. Size and compositional constraints of Ganymede's metallic core for driving an active dynamo. *Icarus* **2009**, *202*, 216–224. [[CrossRef](#)]
13. Schubert, G.; Zhang, K.; Kivelson, M.G.; Anderson, J.D. The magnetic field and internal structure of Ganymede. *Nature* **1996**, *384*, 544–545. [[CrossRef](#)]
14. Verhoogen, J. *Energetics of the Earth*; National Academy Press: Washington, DC, USA, 1980.
15. Hirose, K.; Morard, G.; Sinmyo, R.; Umemoto, K.; Hernlund, J.; Helffrich, G.; Labrosse, S. Crystallization of silicon dioxide and compositional evolution of the Earth's core. *Nature* **2017**, *543*, 99. [[CrossRef](#)] [[PubMed](#)]

16. O'Rourke, J.G.; Stevenson, D.J. Powering Earth's dynamo with magnesium precipitation from the core. *Nature* **2016**, *529*, 387. [[CrossRef](#)] [[PubMed](#)]
17. Du, Z.; Jackson, C.; Bennett, N.; Driscoll, P.; Deng, J.; Lee, K.M.; Greenberg, E.; Prakapenka, V.B.; Fei, Y. Insufficient energy from MgO exsolution to power early geodynamo. *Geophys. Res. Lett.* **2017**, *44*, 11376–11381. [[CrossRef](#)]
18. Badro, J.; Aubert, J.; Hirose, K.; Nomura, R.; Blanchard, I.; Borensztajn, S.; Siebert, J. Magnesium partitioning between Earth's mantle and core and its potential to drive an early exsolution geodynamo. *Geophys. Res. Lett.* **2018**, *45*, 13240–13248. [[CrossRef](#)]
19. Gomi, H.; Ohta, K.; Hirose, K.; Labrosse, S.; Caracas, R.; Verstraete, M.J.; Hernlund, J.W. The high conductivity of iron and thermal evolution of the Earth's core. *Phys. Earth Planet. Inter.* **2013**, *224*, 88–103. [[CrossRef](#)]
20. Ohta, K.; Kuwayama, Y.; Hirose, K.; Shimizu, K.; Ohishi, Y. Experimental determination of the electrical resistivity of iron at Earth's core conditions. *Nature* **2016**, *534*, 95–98. [[CrossRef](#)] [[PubMed](#)]
21. Silber, R.E.; Secco, R.A.; Yong, W.; Littleton, J.A. Electrical resistivity of liquid Fe to 12 GPa: Implications for heat flow in cores of terrestrial bodies. *Sci. Rep.* **2018**, *8*, 10758. [[CrossRef](#)] [[PubMed](#)]
22. Williams, Q. The thermal conductivity of Earth's core: A key geophysical parameter's constraints and uncertainties. *Annu. Rev. Earth Planet. Sci.* **2018**, *46*, 47–66. [[CrossRef](#)]
23. Stacey, F.D.; Anderson, O.L. Electrical and thermal conductivities of Fe–Ni–Si alloy under core conditions. *Phys. Earth Planet. Inter.* **2001**, *124*, 153–162. [[CrossRef](#)]
24. Stacey, F.D.; Loper, D.E. A revised estimate of the conductivity of iron alloy at high pressure and implications for the core energy balance. *Phys. Earth Planet. Inter.* **2007**, *161*, 13–18. [[CrossRef](#)]
25. Konôpková, Z.; McWilliams, R.S.; Gómez-Pérez, N.; Goncharov, A.F. Direct measurement of thermal conductivity in solid iron at planetary core conditions. *Nature* **2016**, *534*, 99.
26. Pozzo, M.; Davies, C.; Gubbins, D.; Alfe, D. Thermal and electrical conductivity of iron at Earth's core conditions. *Nature* **2012**, *485*, 355–358. [[CrossRef](#)]
27. De Koker, N.; Steinle-Neumann, G.; Vlček, V. Electrical resistivity and thermal conductivity of liquid Fe alloys at high P and T, and heat flux in Earth's core. *Proc. Natl. Acad. Sci. USA* **2012**, *109*, 4070–4073. [[CrossRef](#)] [[PubMed](#)]
28. Wagle, F.; Steinle-Neumann, G. Electrical resistivity discontinuity of iron along the melting curve. *Geophys. J. Int.* **2017**, *213*, 237–243. [[CrossRef](#)]
29. Ezenwa, I.C.; Secco, R.A. Invariant electrical resistivity of Co along melting boundary. *Earth Planet. Sci. Lett.* **2017**, *474*, 120–127. [[CrossRef](#)]
30. Silber, R.E.; Secco, R.A.; Yong, W. Constant electrical resistivity of Ni along the melting boundary up to 9 GPa. *J. Geophys. Res. Solid Earth* **2017**, *122*, 5064–5081. [[CrossRef](#)]
31. Secco, R.A.; Schloessin, H.H. The electrical resistivity of solid and liquid Fe at pressures up to 7 GPa. *J. Geophys. Res. Solid Earth* **1989**, *94*, 5887–5894. [[CrossRef](#)]
32. Deng, L.; Seagle, C.; Fei, Y.; Shahar, A. High pressure and temperature electrical resistivity of iron and implications for planetary cores. *Geophys. Res. Lett.* **2013**, *40*, 33–37. [[CrossRef](#)]
33. Pommier, A. Influence of sulfur on the electrical resistivity of a crystallizing core in small terrestrial bodies. *Earth Planet. Sci. Lett.* **2018**, *496*, 37–46. [[CrossRef](#)]
34. Landrum, G.A.; Dronskowski, R. The orbital origins of magnetism: From atoms to molecules to ferromagnetic alloys. *Angew. Chem. Int. Ed.* **2000**, *39*, 1560–1585. [[CrossRef](#)]
35. Mott, N.F. The electrical conductivity of transition metals. *Proc. R. Soc. Lond. A Math. Phys. Eng. Sci.* **1936**, *153*, 699–717.
36. Matula, R.A. Electrical resistivity of copper, gold, palladium, and silver. *J. Phys. Chem. Ref. Data* **1979**, *8*, 1147–1298. [[CrossRef](#)]
37. Powell, R.W.; Tye, R.P. The promise of platinum as a high temperature thermal conductivity reference material. *Br. J. Appl. Phys.* **1963**, *14*, 662. [[CrossRef](#)]
38. Güntherodt, H.J.; Hauser, E.; Künzi, H.U.; Müller, R. The electrical resistivity of liquid Fe, Co, Ni and Pd. *Phys. Lett. A* **1975**, *54*, 291–292. [[CrossRef](#)]
39. Laubitz, M.J.; Matsumura, T. Transport properties of the ferromagnetic metals. I. Cobalt. *Can. J. Phys.* **1973**, *51*, 1247–1256. [[CrossRef](#)]
40. Laubitz, M.J.; Matsumura, T.; Kelly, P.J. Transport properties of the ferromagnetic metals. II. Nickel. *Can. J. Phys.* **1976**, *54*, 92–102. [[CrossRef](#)]

41. Seydel, U.; Fucke, W. Sub-microsecond pulse heating measurements of high temperature electrical resistivity of the 3d-transition metals iron, cobalt, and nickel. *Chem. Inf.* **1977**, *32*, 994–1002. [[CrossRef](#)]
42. Chu, T.K.; Chi, T.C. McGraw-Hill/CICADAS data series on materials properties. In *Properties of Selected Ferrous Alloying Elements, Vol. III-1*; Touloukian, Y.S., Ho, C.Y., Eds.; McGraw-Hill: New York, NY, USA, 1981.
43. Campbell, I.A.; Fert, A. Chapter 9 Transport properties of ferromagnets. In *Handbook of Ferromagnetic Materials*; Wohlfarth, E.P., Ed.; Elsevier: Amsterdam, The Netherlands, 1982; pp. 747–804.
44. Gold, A.V. Review paper: Fermi surfaces of the ferromagnetic transition metals. *J. Low Temp. Phys.* **1974**, *16*, 3–42. [[CrossRef](#)]
45. Coleman, R.V.; Morris, R.C.; Sellmyer, D.J. Magnetoresistance in Iron and Cobalt to 150 kOe. *Phys. Rev. B* **1973**, *8*, 317–331. [[CrossRef](#)]
46. Angadi, M.A.; Fawcett, E.; Rasolt, M. High field magnetoresistance and quantum oscillations in iron whiskers. *Can. J. Phys.* **1975**, *53*, 284–298. [[CrossRef](#)]
47. Himpsel, F.J.; Heimann, P.; Eastman, D.E. Band structure measurements and multi-electron effects (satellites) for nearly-filled d-band metals: Fe, Co, Ni, Cu, Ru, and Pd. *J. Appl. Phys.* **1981**, *52*, 1658–1663. [[CrossRef](#)]
48. Eastman, D.E.; Himpsel, F.J.; Knapp, J.A. Experimental exchange-split energy-band dispersions for Fe, Co, and Ni. *Phys. Rev. Lett.* **1980**, *44*, 95–98. [[CrossRef](#)]
49. Korenman, V.; Prange, R.E. Local-band-theory analysis of spin-polarized, angle-resolved photoemission spectroscopy. *Phys. Rev. Lett.* **1984**, *53*, 186–189. [[CrossRef](#)]
50. Chikazumi, S.; Graham, C.D. *Physics of Ferromagnetism 2e (No. 94)*; Oxford University Press: Oxford, UK, 2009.
51. Iota, V.; Klepeis, J.H.P.; Yoo, C.S.; Lang, J.; Haskel, D.; Srajer, G. Electronic structure and magnetism in compressed 3d transition metals. *Appl. Phys. Lett.* **2007**, *90*, 042505. [[CrossRef](#)]
52. Ross, M.; Boehler, R.; Errandonea, D. Melting of transition metals at high pressure and the influence of liquid frustration: The late metals Cu, Ni, and Fe. *Phys. Rev. B* **2007**, *76*, 184117. [[CrossRef](#)]
53. McMahan, A.K.; Albers, R.C. Insulating nickel at a pressure of 34 TPa. *Phys. Rev. Lett.* **1982**, *49*, 1198. [[CrossRef](#)]
54. McMahan, A.K. Pressure effects on the electronic structure of 4f and 5f materials. *J. Less Common Met.* **1989**, *149*, 1–11. [[CrossRef](#)]
55. Gaspari, G.D.; Gyorffy, B.L. Electron-phonon interactions, d resonances, and superconductivity in transition metals. *Phys. Rev. Lett.* **1972**, *28*, 801–805. [[CrossRef](#)]
56. Brown, J.S. D resonance calculation of the resistivity and thermopower of liquid Ni and Pd. *J. Phys. F Met. Phys.* **1973**, *3*, 1003–1007. [[CrossRef](#)]
57. Shvets, V.T. Influence of sd hybridization of the electrical conductivity of liquid transition metals. *Theor. Math. Phys.* **1982**, *53*, 1040–1046. [[CrossRef](#)]
58. Shvets, V.T.; Savenko, S.; Datsko, S. Perturbation theory for electrical resistivity of liquid transition metals. *Condens. Matter Phys* **2002**, *5*, 511–522. [[CrossRef](#)]
59. McWilliams, R.S.; Konôpková, Z.; Goncharov, A.F. A flash heating method for measuring thermal conductivity at high pressure and temperature: Application to Pt. *Phys. Earth Planet. Inter.* **2015**, *247*, 17–26. [[CrossRef](#)]
60. Silber, R.E.; Secco, R.A.; Yong, W.; Littleton, J.A. Heat flow in Earth's core from invariant electrical resistivity of Fe-Si on the melting boundary to 9 GPa: Do light elements matter? *J. Geophys. Res. Solid Earth* **2019**, *124*. [[CrossRef](#)]
61. Ezenwa, I.C.; Secco, R.A.; Yong, W.; Pozzo, M.; Alfè, D. Electrical resistivity of solid and liquid Cu up to 5GPa: Decrease along the melting boundary. *J. Phys. Chem. Solids* **2017**, *110*, 386–393. [[CrossRef](#)]
62. Littleton, J.A.; Secco, R.A.; Yong, W. Decreasing electrical resistivity of silver along the melting boundary up to 5 GPa. *High Press. Res.* **2018**, *38*, 99–106. [[CrossRef](#)]
63. Berrada, M.; Secco, R.A.; Yong, W. Decreasing electrical resistivity of gold along the melting boundary up to 5 GPa. *High Press. Res.* **2018**, *38*, 367–376. [[CrossRef](#)]
64. Ezenwa, I.C.; Secco, R.A. Constant electrical resistivity of Zn along the melting boundary up to 5 GPa. *High Press. Res.* **2017**, *37*, 319–333. [[CrossRef](#)]
65. Klemens, P.G.; Williams, R.K. Thermal conductivity of metals and alloys. *Int. Met. Rev.* **1986**, *31*, 197–215. [[CrossRef](#)]
66. Breuer, D.; Rueckriemen, T.; Spohn, T. Iron snow, crystal floats, and inner-core growth: Modes of core solidification and implications for dynamos in terrestrial planets and moons. *Prog. Earth Planet. Sci.* **2015**, *2*, 39. [[CrossRef](#)]

67. Secco, R.A. Thermal conductivity and Seebeck coefficient of Fe and Fe-Si alloys: Implications for variable Lorenz number. *Phys. Earth Planet. Inter.* **2017**, *265*, 23–34. [[CrossRef](#)]
68. Sohl, F.; Spohn, T.; Breuer, D.; Nagel, K. Implications from Galileo observations on the interior structure and chemistry of the Galilean satellites. *Icarus* **2002**, *157*, 104–119. [[CrossRef](#)]
69. Rivoldini, A.; Van Hoolst, T. The interior structure of Mercury constrained by the low-degree gravity field and the rotation of Mercury. *Earth Planet. Sci. Lett.* **2013**, *377*, 62–72. [[CrossRef](#)]
70. Desai, P.D. Thermodynamic properties of iron and silicon. *J. Phys. Chem. Ref. Data* **1986**, *15*, 967–983. [[CrossRef](#)]
71. Hussmann, H.; Sotin, C.; Lunine, J.I. Interiors and evolution of icy satellites. In *Treatise on Geophysics*; Schubert, G., Ed.; Elsevier: Amsterdam, The Netherlands, 2007; Volume 10.
72. Jeanloz, R. Properties of iron at high pressures and the state of the core. *J. Geophys. Res. Solid Earth* **1979**, *84*, 6059–6069. [[CrossRef](#)]
73. Schubert, G.; Anderson, J.D.; Spohn, T.; McKinnon, W.B. Interior composition, structure and dynamics of the Galilean satellites. *Jupit. Planet Satell. Magnetos.* **2004**, *1*, 281–306.



© 2019 by the authors. Licensee MDPI, Basel, Switzerland. This article is an open access article distributed under the terms and conditions of the Creative Commons Attribution (CC BY) license (<http://creativecommons.org/licenses/by/4.0/>).